COMPARISON OF RESOLUTION FUNCTIONS OF 3-D MULTI-COMPONENT AND 3-D SINGLE-COMPONENT IMAGING ALGORITHMS FOR GROUND PENETRATING RADAR DATA.

J. van der Kruk, C.P.A. Wapenaar, J.T. Fokkema

Section of Applied Geophysics and Petrophysics, Department of Applied Earth Sciences,
Delft University of Technology, Mijnbouwstraat 120, 2628 RX Delft, The Netherlands

ABSTRACT

For electromagnetic imaging the vectorial character of the emitted field and the radiation characteristics of the source and the receiver play an important role. The scalar imaging algorithms, such as Synthetic Aperture Radar (SAR) and the Gazdag phase shift, are commonly used to image GPR data, but are originally developed for the imaging of scalar seismic reflections and thus do not take into account the vectorial character and the radiation characteristics of the source and receiver antennas. An analytical discussion is presented about the imaging of a point scatterer present in a homogeneous space using a zero-offset configuration. For a single frequency component this results in a resolution function. Due to the closed-form expressions for the forward and inverse wave field extrapolators, closed-form expressions are obtained for these resolution functions. Both scalar inverse wave field extrapolators do not represent the point scatterer adequately and motivate the introduction of modified scalar inverse wave field extrapolators. Still, the modified SAR and Gazdag extrapolators do not result in a circular symmetric resolution function, which is the expected representation of a point scatterer.

To obtain a stable inverse wave field extrapolator based on the electromagnetic scattering formalism, it is necessary to combine two orthogonal components of the measured scattered electric field, which leads to a multi-component imaging algorithm. The multi-component imaging algorithm results in a circular symmetric resolution function, which represents the point scatterer adequately. For two homogeneous halfspaces it is not feasible to carry out a similar analytical approach. However, in numerical sense the same procedure can be carried out, which has the important benefit that also the offset between the source and receiver can be taken into account. Numerical results are presented for two homogeneous halfspaces and imaging results of experiments are presented, which take into account the vectorial character of the measured electric field, the offset between the source and receiver and the presence of a dielectric homogeneous halfspace.

KEY WORDS: 3D imaging, ground penetrating radar, resolution function

INTRODUCTION

Commonly used imaging strategies for GPR data used in the literature are similar to the (scalar) seismic imaging algorithms, of which we will discuss two; the SAR imaging algorithm and the Gazdag phase shift method. These algorithms are compared with the multi-component imaging algorithm (van der Kruk et al., 2000). Note that the SAR and Gazdag imaging algorithms are based on the seismic scalar scattering representation. Kagalenko and Weedon (1996) compared the imaging results using the Gazdag phase shift and the SAR imaging algorithms for a two-dimensional configuration using numerical modelling of a point scatterer and showed that the Gazdag phase shift resulted in a higher image resolution and less artifacts compared with the SAR imaging. Gunawardena and Longstaff (1998) formulated a wave equation based SAR algorithm which is equal to the Kirchhoff migration algorithm (Schneider, 1978). The multi-component imaging algorithm is based on the vectorial electromagnetic scattering representation, which results in a more representative image of the scatterer compared with scalar imaging algorithms.

An imaging algorithm basically consists of two steps; the first step eliminates propagation effects for each separate frequency component (inverse wave field extrapolation). The second step involves a time zero selection for each position, which is carried out by adding all (positive and negative) frequencies. This operation is known as the imaging principle (Claerbout, 1971 and Berkhout, 1981). For all discussed migration algorithms, the imaging principle is equivalent. The discussion of the inverse wave field extrapolators is thus our main concern. To investigate the performance of scalar inverse extrapolators and to derive systematically a stable inverse extrapolator dedicated to the electromagnetic case we first discuss the forward wave field extrapolation.

TWO-WAY WAVE FIELD EXTRAPOLATOR

The linearized expression for the scattering formalism, based on the Born approximation, is given by

$$\hat{E}^s_\alpha(\boldsymbol{x}^R,\omega) = \int\limits_{\boldsymbol{x}^c\in\mathbb{D}^c} \hat{G}^{\mathrm{EJ}}_{\alpha r}(\boldsymbol{x}^R|\boldsymbol{x}^c,\omega)\chi^{\hat{\eta}}(\boldsymbol{x}^c) \times \hat{G}^{\mathrm{EJ}}_{r\beta}(\boldsymbol{x}^c|\boldsymbol{x}^S,\omega)\hat{J}_\beta(\boldsymbol{x}^S,\omega)\mathrm{d}V, \quad (1)$$

where $\mathbb{D}^c$ is the scattering domain and Einstein's summation convention applies to repeated subscripts. The Latin subscript r can take the values $\{1,2,3\}$, whereas the Greek subscripts can take the values $\{\alpha,\beta\} = \{1,2\}$. $\hat{G}^{\mathrm{EJ}}_{r\beta}$ describes the propagation of the vectorial electric field due to a point source $\hat{J}_\beta$, to the location of the contrast $\chi^{\hat{\eta}}$ at position $\boldsymbol{x}^c$. This scatterer can be considered as a secondary source and the propagation from $\boldsymbol{x}^c$ towards the receiver is described by $\hat{G}^{\mathrm{EJ}}_{\alpha r}$. The contrast $\chi^{\hat{\eta}}$ is defined as $\chi^{\hat{\eta}} = \hat{\eta}^s - \hat{\eta}$, where $\hat{\eta}$ and $\hat{\eta}^s$ describe the properties of the background and the scatterer, respectively. $\hat{\eta}$ is defined as $\hat{\eta} = \sigma + j\omega\varepsilon$. In Figure 1 the configuration of the four possible source receiver setups is depicted. To make an analytical discussion possible we will first determine the forward wave field extrapolators in a homogeneous space for a zero-offset configuration, with $\boldsymbol{x}^S{=}\boldsymbol{x}^R{=}\boldsymbol{x}^M{=}(x_1^M, x_2^M, 0)$.

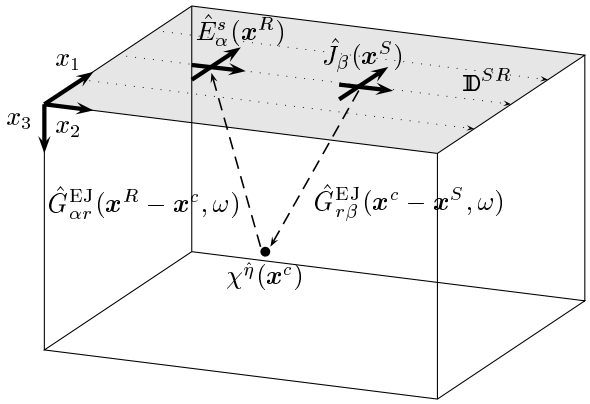

Figure 1. The configuration of the four possible source receiver setups.

It is convenient to combine the propagation of the vector electric field from the source towards the scatterer and from the scatterer back to the receiver by introducing the wave field extrapolator $\hat{D}_{\alpha\beta}$, which describes the inner product between the two Green's functions. Writing $\hat{J}_\beta(\boldsymbol{x}^S,\omega)$ as $\hat{S}(\omega)$, Eq. (1) can be rewritten as

$$\hat{E}_{\alpha\beta}(\boldsymbol{x}^M,\omega) = \hat{S}(\omega)\int\limits_{\boldsymbol{x}^c\in\mathbb{D}^c} \hat{D}_{\alpha\beta}(\boldsymbol{x}^M{-}\boldsymbol{x}^c,\omega)\chi^{\hat{\eta}}(\boldsymbol{x}^c)\mathrm{d}V, \quad (2)$$

where the wave field extrapolator $\hat{D}_{\alpha\beta}$ is given by

$$\begin{aligned}\hat{D}_{\alpha\beta}&(\boldsymbol{x}^M - \boldsymbol{x}^c,\omega)\\ &= \hat{G}^{\mathrm{EJ}}_{\alpha r}(\boldsymbol{x}^M - \boldsymbol{x}^c,\omega)\hat{G}^{\mathrm{EJ}}_{\beta r}(\boldsymbol{x}^M - \boldsymbol{x}^c,\omega),\\ &= \hat{G}^{\mathrm{EJ}}_{\alpha r}(\boldsymbol{x}^M - \boldsymbol{x}^c,\omega)\hat{G}^{\mathrm{EJ}}_{r\beta}(\boldsymbol{x}^c - \boldsymbol{x}^M,\omega). \quad (3)\end{aligned}$$

The wave field extrapolator $\hat{D}_{\alpha\beta}$ will be denoted as the two-way wave field extrapolator, whereas it describes the inner product of the Green's function describing the downward propagation from source towards scatterer and the Green's function describing the upward propagation from scatterer towards receiver. The expression for $\hat{G}^{\mathrm{EJ}}_{kr}(\boldsymbol{x},\omega)$ is given by

$$\hat{G}^{\mathrm{EJ}}_{kr}(\boldsymbol{x},\omega) = \hat{\eta}^{-1}[\partial_k\partial_r + k^2\delta_{kr}]\hat{G}(R,\omega), \quad (4a)$$

$$\hat{G}(R,\omega) = \frac{\exp(-jkR)}{4\pi R}, \quad (4b)$$

$$R = |\boldsymbol{x}|, \quad (4c)$$

$$k = \frac{\omega}{c}. \quad (4d)$$

The two-way wave field extrapolator can be rewritten by separating the phase delay and the corresponding amplitude factor as

$$\begin{aligned}\hat{D}_{\alpha\beta}(\boldsymbol{x},\omega) &= \hat{G}^{\mathrm{EJ}}_{\alpha r}(\boldsymbol{x},\omega)\hat{G}^{\mathrm{EJ}}_{\beta r}(\boldsymbol{x},\omega),\\ &= \hat{A}_{\alpha\beta}(\boldsymbol{x},\omega)\exp(-2jkR). \quad (5)\end{aligned}$$

Because the wave field extrapolator in Eq. (5) is derived for a zero-offset measurement a factor 2 occurs in the two-way phase delay $\exp(-2jkR)$, which indicates that the wave field has traveled twice along the same path. The separate elements of $\hat{A}_{\alpha\beta}$ in Eq. (5) are evaluated for the far field contributions using Eqs. (4a)-(4d) and can be written as

$$\hat{A}_{11}(\boldsymbol{x},\omega) = \frac{R^2 - x_1^2}{R^4}C(\omega), \quad (6a)$$

$$\hat{A}_{12}(\boldsymbol{x},\omega) = -\frac{x_1x_2}{R^4}C(\omega), \quad (6b)$$

$$\hat{A}_{21}(\boldsymbol{x},\omega) = -\frac{x_1x_2}{R^4}C(\omega), \quad (6c)$$

$$\hat{A}_{22}(\boldsymbol{x},\omega) = \frac{R^2 - x_2^2}{R^4}C(\omega), \quad (6d)$$

where

$$C(\omega) = \frac{k^4}{\hat{\eta}^2(4\pi)^2}. \quad (7)$$

Because the Gazdag extrapolator and the multi-component inverse extrapolator are defined in the spatial Fourier domain, the forward extrapolator is transformed to the spatial Fourier domain. Using Eq. (5) we obtain

$$\tilde{D}_{\alpha\beta}(k_1,k_2,x_3,\omega) = \int\limits_{(x_1,x_2)\in\mathbb{R}^2} \hat{A}_{\alpha\beta}(\boldsymbol{x},\omega)\exp[j\phi(\boldsymbol{x})]\mathrm{d}A, \quad (8)$$

where

$$\phi(\boldsymbol{x}) = -2kR + k_1x_1 + k_2x_2. \quad (9)$$

Using the method of stationary phase, Eq. (8) can be approximated for large ϕ. The expression for $\tilde{D}_{\alpha\beta}(k_1,k_2,x_3,\omega)$ is obtained as

$$\tilde{D}_{\alpha\beta}(k_1,k_2,x_3,\omega) = \tilde{d}_{\alpha\beta}\exp(-jk_3|x_3|), \quad (10)$$

where k_3 is given by

$$k_3 = \begin{cases} \sqrt{4k^2 - k_1^2 - k_2^2}, & \text{for } k_1^2 + k_2^2 \leq 4k^2, \\ -j\sqrt{k_1^2 + k_2^2 - 4k^2}, & \text{for } k_1^2 + k_2^2 > 4k^2, \end{cases} \tag{11}$$

and

$$\tilde{d}_{11}(k_1, k_2, x_3, \omega) = -\frac{2\pi j C(\omega)}{(2k)^3 |x_3|}[(2k)^2 - k_1^2], \tag{12a}$$

$$\tilde{d}_{12}(k_1, k_2, x_3, \omega) = \frac{2\pi j C(\omega)}{(2k)^3 |x_3|} k_1 k_2, \tag{12b}$$

$$\tilde{d}_{21}(k_1, k_2, x_3, \omega) = \frac{2\pi j C(\omega)}{(2k)^3 |x_3|} k_1 k_2, \tag{12c}$$

$$\tilde{d}_{22}(k_1, k_2, x_3, \omega) = -\frac{2\pi j C(\omega)}{(2k)^3 |x_3|}[(2k)^2 - k_2^2]. \tag{12d}$$

Note that the method of stationary phase can also be applied to evaluate the inverse spatial Fourier transformation.

SCALAR INVERSE WAVE FIELD EXTRAPOLATORS

The inverse wave field extrapolator for the SAR imaging algorithm is defined in the spatial domain and is the complex conjugate of only the phase shift term given in Eq. (5). In seismics this imaging algorithm is known as diffraction summation migration. The inverse wave field extrapolator, which forms the basis of Gazdag phase-shift imaging, (see Eq. (45) of Gazdag, 1978), is defined in the spatial Fourier domain and is the complex conjugate of only the phase shift term given in Eq. (10). The method of stationary phase is used to derive an expression for the SAR inverse extrapolator in the spatial Fourier domain and an expression for the Gazdag inverse extrapolator in the space domain. The SAR and the Gazdag inverse extrapolators are thus given in the space Fourier domain by

$$\hat{H}^{gd} = \frac{-jk|x_3|}{\pi R^2} \exp(2jkR), \tag{13}$$

$$\hat{H}^{sar} = \exp(j2kR), \tag{14}$$

respectively, whereas in the spatial Fourier domain they are given by

$$\tilde{H}^{gd} = \exp(jk_3^*|x_3|), \tag{15}$$

$$\tilde{H}^{sar} = \frac{4\pi jk|x_3|}{(k_3^*)^2} \exp(jk_3^*|x_3|). \tag{16}$$

Here * denotes complex conjugate. Note that with k_3 defined in Eq. (11), the term $\exp(jk_3^*|x_3|)$ is stable for all k_1 and k_2.

The Gazdag and SAR extrapolators are basically a phase shift in the spatial Fourier domain and in the space domain, respectively. Both extrapolators do not take into account the vectorial character and the radiation characteristics of the source and receiver antennas.

Next, an approximate inverse is derived for each separate component of the forward wave field extrapolator. The single-component two-way wave field extrapolators $\tilde{D}_{\alpha\beta}(k_1, k_2, x_3, \omega)$ as given in Eqs. (10)-(12d) are inverted in the spatial Fourier domain. Using the stationary phase approximation the expressions in the space domain for the scalar inverse wave field extrapolators are obtained:

$$\hat{H}_{11} = \frac{-R^2}{R^2 - x_1^2} \frac{\exp(2jkR)}{\pi^2 C}, \tag{17a}$$

$$\hat{H}_{12} = \frac{-R^2}{x_1 x_2} \frac{\exp(2jkR)}{\pi^2 C}, \tag{17b}$$

$$\hat{H}_{21} = \frac{-R^2}{x_1 x_2} \frac{\exp(2jkR)}{\pi^2 C}, \tag{17c}$$

$$\hat{H}_{22} = \frac{-R^2}{R^2 - x_2^2} \frac{\exp(2jkR)}{\pi^2 C}. \tag{17d}$$

$\hat{H}_{11}$ is not stable near the x_1-axis. This is already indicated by the forward wave field extrapolator in Eq. (6a), which has a small sensitivity for scatterers near the x_1-axis. This is caused by the fact that the radiation characteristic of a horizontal dipole oriented in the x_1-direction has a zero at the x_1-axis. Similar conclusions can be drawn for the other single-component inverse wave field extrapolators Eqs (17b)-(17d).

In conclusion, we can say that single-component inverse wave field extrapolation based on the two-way wave field extrapolator for a homogeneous space is not stable and that the inverse wave field extrapolation has to be carried out by combining more components of the measured scattered electric field.

MULTI-COMPONENT INVERSE WAVE FIELD EXTRAPOLATOR

To combine more components of the emitted and measured electric field, a tensorial forward wave field extrapolator is introduced, where each element represents the far field expression of the scattering formalism for a specific source-receiver combination. Similar to Eqs. (2) and (5) we can write for the zero-offset scattering mechanism

$$\hat{\mathbf{E}}(\boldsymbol{x}^M, \omega) = \hat{S}(\omega) \int_{\boldsymbol{x}^c \in \mathbb{D}^c} \hat{\mathbf{D}}(\boldsymbol{x}^M - \boldsymbol{x}^c, \omega) \chi^{\hat{\eta}}(\boldsymbol{x}^c) \mathrm{d}V, \tag{18}$$

where $\hat{\mathbf{E}}(\boldsymbol{x}^M, \omega)$ is given by

$$\hat{\mathbf{E}}(\boldsymbol{x}^M, \omega) = \begin{bmatrix} \hat{E}_{11} & \hat{E}_{12} \\ \hat{E}_{21} & \hat{E}_{22} \end{bmatrix} (\boldsymbol{x}^M, \omega), \tag{19}$$

and $\hat{\mathbf{D}}(\boldsymbol{x}, \omega)$ is the tensorial 3-D two-way wave field extrapolator for zero-offset, which is given by

$$\hat{\mathbf{D}}(\boldsymbol{x}, \omega) = \hat{\mathbf{A}}(\boldsymbol{x}, \omega) \exp(-2jkR), \tag{20}$$

where

$$\hat{\mathbf{A}}(\boldsymbol{x},\omega) = \begin{bmatrix} \hat{A}_{11} & \hat{A}_{12} \\ \hat{A}_{21} & \hat{A}_{22} \end{bmatrix} (\boldsymbol{x},\omega), \tag{21}$$

and $\hat{A}_{\alpha\beta}$ are given by Eqs. (6a)-(6d). Combining Eqs. (10) and (12a)-(12d) the expression for $\tilde{\mathbf{D}}(k_1,k_2,x_3,\omega)$ is obtained as

$$\tilde{\mathbf{D}}(k_1,k_2,x_3,\omega) = \tilde{\mathbf{d}}(k_1,k_2,x_3,\omega)\exp(-jk_3|x_3|), \tag{22}$$

where

$$\tilde{\mathbf{d}}(k_1,k_2,x_3,\omega) = \frac{-2\pi jC(\omega)}{(2k)^3|x_3|}\begin{bmatrix} (2k)^2-k_1^2 & -k_1k_2 \\ -k_1k_2 & (2k)^2-k_2^2 \end{bmatrix}. \tag{23}$$

To obtain an approximate inverse of the multi-component 3-D two-way wave field extrapolator $\tilde{\mathbf{D}}(k_1,k_2,x_3,\omega)$, we take the complex conjugate of the exponent and the matrix inverse of the matrix in Eq. (23), which results in

$$\tilde{\mathbf{H}}(k_1,k_2,x_3,\omega) = \tilde{\mathbf{h}}(k_1,k_2,x_3,\omega)\exp(jk_3^*|x_3|), \tag{24}$$

where

$$\tilde{\mathbf{h}}(k_1,k_2,x_3,\omega) = \frac{jk|x_3|}{\pi C(\omega)k_3^2}\begin{bmatrix} (2k)^2-k_2^2 & k_1k_2 \\ k_1k_2 & (2k)^2-k_1^2 \end{bmatrix}. \tag{25}$$

Using the stationary phase approximation, the spatial equivalent of Eqs. (24) and (25) is obtained as

$$\hat{\mathbf{H}} = \frac{4k^2}{4\pi^2 C(\omega)}\begin{bmatrix} (R^2-x_2^2)/R^2 & x_1x_2/R^2 \\ x_1x_2/R^2 & (R^2-x_1^2)/R^2 \end{bmatrix} \times \exp(2jkR). \tag{26}$$

Note that this multi-component inverse wave field extrapolator is stable.

SPATIAL RESOLUTION FUNCTIONS

The performance of the scalar and multi-component 3-D inverse wave field extrapolators is investigated by analysing the imaging result of a point scatterer for one single frequency component, which is denoted as the spatial resolution function. In this way the performance of the inverse wave field extrapolator can be analysed thoroughly.

First, the spatial resolution is investigated for a point scatterer present in a homogeneous domain using a zero-offset configuration. The closed-form expressions for the forward and inverse wave field extrapolators in the space domain and the spatial Fourier domain enable the derivation of closed-form expressions for the spatial resolution function. In this way an analytical check of the performance of the inverse wave field extrapolators can be carried out.

For the special situation of one diffraction point only at position $\boldsymbol{x}^d$, having a real-valued contrast with unit amplitude, according to

$$\chi^{\hat{\eta}}(\boldsymbol{x}) = \delta(\boldsymbol{x}-\boldsymbol{x}^d), \tag{27}$$

the measured electric field may be expressed in terms of the source function $\hat{S}(\omega)$, according to (See Eq. (18))

$$\hat{\mathbf{E}}(\boldsymbol{x}^M,\omega) = \hat{S}(\omega)\hat{\mathbf{D}}(\boldsymbol{x}^M-\boldsymbol{x}^d,\omega). \tag{28}$$

In the following we consider for convenience a source function with unit amplitude. The expression for the bandlimited version of the contrast at the depth level x_3^d reads

$$\langle\hat{\chi}(\boldsymbol{x},\omega)\mathbf{I}\rangle = \int_{(x_1^M,x_2^M)\in\mathbb{R}^2} \hat{\mathbf{H}}(\boldsymbol{x}-\boldsymbol{x}^M,\omega)\hat{\mathbf{D}}(\boldsymbol{x}^M-\boldsymbol{x}^d,\omega)\mathrm{d}A, \tag{29}$$

with $\boldsymbol{x} = (x_1,x_2,x_3^d)$. Using some basic results of Fourier theory, we may express Eq. (29) in terms of the Fourier transforms of $\hat{\mathbf{H}}$ and $\hat{\mathbf{D}}$, according to

$$\langle\hat{\chi}(\boldsymbol{x},\omega)\mathbf{I}\rangle = \frac{1}{4\pi^2}\int_{(k_1,k_2)\in\mathbb{R}^2} \tilde{\mathbf{H}}(k_1,k_2,x_3^d,\omega)\tilde{\mathbf{D}}(k_1,k_2,x_3^d,\omega) \times \exp[-j(k_1\{x_1-x_1^d\}+k_2\{x_2-x_2^d\})]\mathrm{d}A. \tag{30}$$

$\tilde{\mathbf{D}}$ is given by Eqs. (22) and (23). $\tilde{\mathbf{H}}$ is given by Eqs. (24) and (25).

Next, we evaluate Eq. (30) by ignoring the erroneous contribution of the evanescent waves. This is done most conveniently if we introduce polar coordinates. Hence, from Eq. (30) we now obtain Eq. (31) below. Due to the suppression of the evanescent waves the maximum radial spatial frequency component equals $2k$. Eq. (31) can be simply be rewritten for the single-component inverse wave field extrapolators, yielding Eq. (32) below.

$$\langle\hat{\chi}(r,\phi,x_3^d,\omega)\mathbf{I}\rangle = \frac{1}{4\pi^2}\int_{\kappa=0}^{2k}\left(\int_{\theta=0}^{2\pi}\tilde{\mathbf{h}}(\kappa,\theta,x_3^d,\omega)\tilde{\mathbf{d}}(\kappa,\theta,x_3^d,\omega)\exp[-j\kappa r\cos(\theta)]\mathrm{d}\theta\right)\kappa\mathrm{d}\kappa, \tag{31}$$

$$\hat{\chi}_{\alpha\beta}(r,\phi,x_3^d,\omega) = \frac{1}{4\pi^2}\int_{\kappa=0}^{2k}\left(\int_{\theta=0}^{2\pi}\tilde{h}^{\{gd,sar\}}(\kappa,\theta,x_3^d,\omega)\tilde{d}_{\alpha\beta}(\kappa,\theta,x_3^d,\omega)\exp[-j\kappa r\cos(\theta)]\mathrm{d}\theta\right)\kappa\mathrm{d}\kappa, \tag{32}$$

$$\hat{\chi}_{11}^{gd}(r,\phi,x_3^d,\omega) = \frac{-jC}{|x_3^d|}\left(\sin^2(\phi)\frac{J_1(2kr)}{r} + (3\cos^2(\phi)-\sin^2(\phi))\frac{J_2(2kr)}{2kr^2}\right). \tag{33}$$

The Gazdag phase shift method for wave equation migration is denoted by $\tilde{H}_{gd}$ and given by Eq. (15), which can be written as an amplitude factor $\tilde{h}_{gd} = 1$ and a phase shift. Substitution of $\tilde{h}_{gd}$ and $\tilde{d}_{11}$ (Eq. (12a)) into Eq. (32), yields Eq. (33).

Analysing the result in detail we observe that the obtained resolution function is not circular symmetric. The Gazdag filter is a symmetric extrapolator, but the scattered wave field has non-symmetric properties as indicated by Eqs. (5)-(6d). Another drawback of this result is that the amplitude of the resolution function is inversely proportional to the depth of the diffractor, whereas one would expect it to be independent of x_3^d (bear in mind that inverse wave field extrapolation should compensate for the propagation effects).

The SAR inverse extrapolator is denoted by $\tilde{H}_{sar}$ in the spatial Fourier domain and is given by Eq. (16). It is not feasible to obtain a closed-form expression for the resolution function. However, an angle dependent resolution function is obtained, which is not depending on the depth of the diffractor.

Substitution of the multi-component inverse wave field extrapolator given in Eq. (25) and $\tilde{\mathbf{d}}$ given in Eq. (23) into Eq. (31) yields

$$\langle \hat{\chi}(r, \phi, x_3^d)\mathbf{I} \rangle = \frac{2k}{2\pi} \frac{J_1(2kr)}{r} \mathbf{I}. \tag{34}$$

The result for the multi-component imaging is a circular symmetric resolution function.

REVISED SCALAR INVERSE WAVE FIELD EXTRAPOLATORS

An important requirement of an imaging algorithm is to compensate for the propagation effects. The Gazdag inverse wave field extrapolator does not satisfy this requirement. Therefore it is suggested to introduce a revised extrapolator which does compensate for the propagation effects, which is simply achieved by a scaling with x_3^d. Another requirement was that the obtained image represents the scatterer adequately. A representative resolution function should return for a real valued contrast also a real valued resolution function. When we analyse the obtained resolution functions, we observe that the resolution function using the Gazdag extrapolator returns an imaginary resolution function, whereas the SAR extrapolator returns a real-valued resolution function with a negative peak. The multi-component extrapolator returns a real valued resolution function with a positive peak giving a representative image of the point scatterer. The peaks of both scalar extrapolators do not represent the properties of the point scatterer. Therefore modified extrapolators are introduced, which are given in the space domain by

$$\hat{H}_{gd} = \frac{-k|x_3|^2}{\pi R^2} \exp(j2kR), \tag{35}$$

$$\hat{H}_{sar} = -\exp(j2kR), \tag{36}$$

and in the spatial Fourier domain by

$$\tilde{H}_{gd} = -j|x_3| \exp(jk_3^*|x_3|), \tag{37}$$

$$\tilde{H}_{sar} = \frac{-4\pi jk|x_3|}{(k_3^*)^2} \exp(jk_3^*|x_3|). \tag{38}$$

RESOLUTION FUNCTION FOR A POINT SCATTERER IN TWO HOMOGENEOUS HALFSPACES

It is not feasible to derive closed-form expressions for the resolution functions of a point scatterer in a homogeneous halfspace. This is due to the complex radiation characteristics of a horizontal dipole present on a dielectric halfspace. Far field expressions for these radiation characteristics are given by Engheta and Papas (1982). These expressions are used to carry out a numerical analysis to obtain resolution functions for the different inverse wave field extrapolators. In Figure (1) the real and imaginary part of the resolution function using the SAR inverse wave field extrapolator is depicted. In Figure (2) the real and imaginary part of the resolution function using the Gazdag inverse wave field extrapolator is depicted. Both scalar imaging algorithms show a non-circular symmetric resolution function and also show a non-zero imaginary imaged contrast. In Figure (3) the real and imaginary part of the resolution function using the multi-component inverse wave field extrapolator is depicted. The multi-component algorithm represents the point scatterer most appropriately. The multi-component results show the least oscillations in the tails of the resolution function, compared with the scalar imaging algorithms. When an imaginary valued contrast would be present in the subsurface, the multi-component imaging algorithm would result in an imaginary valued resolution function. From these synthetic results it is indicated that using the multi-component imaging algorithm it may be possible to distinguish between different contrasts. Note that an important benefit of the numerical implementation is that also the offset between the source and receiver antennas can be taken into account.

EXPERIMENTAL RESULTS

At a test location several objects were buried in sand. Measurements were made with the 900 MHz pulseEKKO system using different polarisations of the source and receiver antennas. The spatial sampling is 5 cm inline and crossline and the offset between the source and receiver antennas was 30 cm to enable multi-component measurements. Prior to the imaging the time zero was adjusted and the average trace was removed from the data, because the imaging scheme uses only reflected waves and not direct waves. The data were imaged using a relative permittivity of $\varepsilon_r = 3.1$ and was imaged taking into account the

radiation patterns in a dielectric halfspace and the offset between the source and receiver. The source wavelet was not taken into account, but a time zero correction has been applied to obtain an approximate zero phase wavelet. The results were obtained using a combination of the source oriented in the x_1-direction and the receiver oriented in the x_1- and x_2-direction. Surfaces of constant absolute value are plotted for the multi-component imaging results in Figure 4.
Several objects are present at the test site. Objects A, B and C are steel pipes. The length of pipes A and B is 1 meter. In Figure 5 the real, imaginary and absolute amplitudes of the image result are plotted for the different imaging results, along a line crossing object B, which is parallel to the x_1-axis. Note that the imaging principle has been carried out for positive frequencies only. This facilitates an analysis of real and imaginary part of the obtained contrast, separately. The largest amplitude is obtained for the real part of the imaged contrast for all imaging algorithms. Furthermore it is noted that the imaginary part is small between the endpoints of the pipe for the multi-component imaging result compared with the Gazdag and SAR result. Ideally the imaginary part should be zero for steel. The obtained spatial resolution is for the multi-component algorithm better compared with the scalar imaging algorithms. These preliminary results indicate that it may be possible to extract the medium properties from the imaged contrast. A requirement is that the source wavelet is known better and that the radiation characteristics of a finite length antenna are known better. Another fact that is important, is the influence of the intermediate field on the obtained image result. Note that we have used the Born approximation. This also requires attention for the validity of the results obtained.

CONCLUSIONS

The performance of scalar imaging algorithms and the multi-component imaging algorithm were investigated by comparing the results of the imaging of a point scatterer for one single frequency component. For a homogeneous space an analytical discussion has been carried out. For a real-valued contrast the scalar inverse wave field extrapolators do not represent the scatterer adequately, which motivates the introduction of revised scalar inverse wave field extrapolators. Still the scalar imaging results show no longer a circular and symmetric resolution function, which is an indication that the radiation characteristics of the source and receiver still influence the obtained image for conventional scalar imaging schemes. A scalar inverse wave field extrapolator based on the linearised scattering formalism is not stable, which motivates the combination of more components to obtain a stable inverse wave field extrapolator. A combination of the four possible source-receiver combinations facilitates the derivation of a stable multi-component inverse wave field extrapolator. A multi-component electromagnetic image reconstruction technique has been derived, which is based on the vectorial wave equation. The result for the multi-component imaging of a point scatterer in a homogeneous space for one single frequency component is a circular symmetric resolution function. For two homogeneous halfspaces it is not feasible to carry out a similar analytical approach. However, in numerical sense the same procedure can be carried out, which has the important benefit that also the offset between the source and receiver can be taken into account.
Experimental results of the multi-component 3D vectorial electromagnetic imaging scheme have been presented. The radiation patterns on a homogeneous halfspace and the offset between the source and receiver have been taken into account and several objects were correctly imaged. A comparison between the scalar an multi-component imaging algorithms indicate that that it may be possible by using the multi-component imaging algorithm to obtain medium properties of the scatterers.

ACKNOWLEDGEMENTS

This research is supported by the Dutch Technology Foundation (STW), project nr. DMB 3649.

REFERENCES

Berkhout, A.J., 1981, Wave field extrapolation in seismic migration, a tutorial, *Geophysics*, Vol. 46 No. 12, pp. 1638-1656.

Claerbout, J.F., 1971, Toward a unified theory of reflector mapping, *Geophysics*, Vol. 36 pp. 467-481

Engheta, N. and Papas, C.H., 1982, Radiation patterns of interfacial dipole antennas, *Radio Science*, Vol. 17, No. 6, pp. 1557-1566.

Gazdag, J., 1978, Wave equation migration with the phase-shift method, *Geophysics*, **43**, 1342–1351

Gunawardena, A. and Longstaff, D., 1998, Wave equation formulations of synthetic aperture radar (SAR) algorithms in the time-space domain, *IEEE transactions on Geoscience and Remote Sensing* **36**, 1995-1999

Kagalenko, M.B. and Weedon, W.H.,1996, Comparison of backpropagation and synthetic aperture imaging algorithms for processing GPR data, Proceedings of the AP-S International Symposium and URSI Radio Science Meeting. Part 3, 2179-2182

van der Kruk, J., Wapenaar, C.P.A and Fokkema, J.T., 2000, Multi-component 3-D Imaging of ground penetrating radar data using matrix inversion in the spatial Fourier domain, Proceedings Eight international conference on Ground-Penetrating Radar, 508-513.

Schneider, W.A., 1978, Integral formulation for migration in two and three dimensions, *Geophysics*, **43**, 49-76.

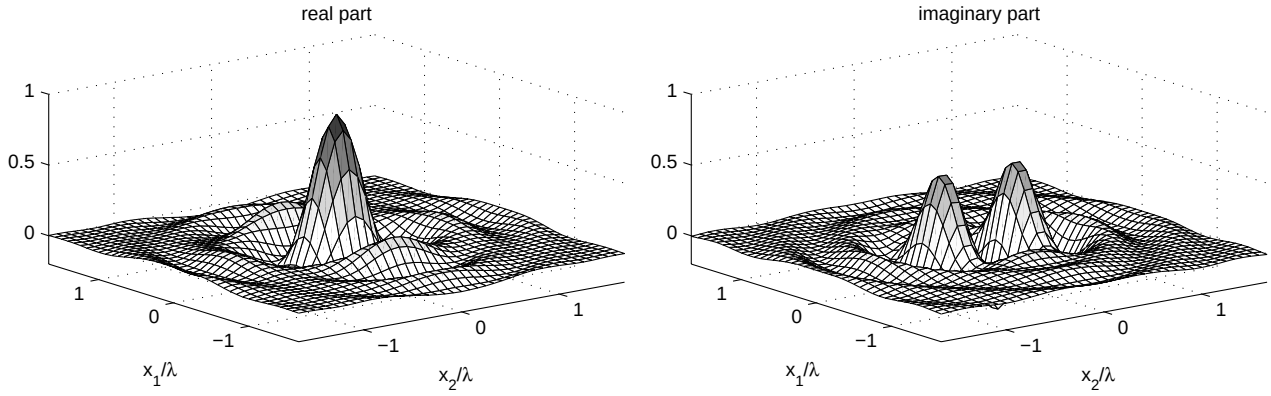

Figure 1: Real and imaginary part of the resolution function using the modified SAR imaging algorithm

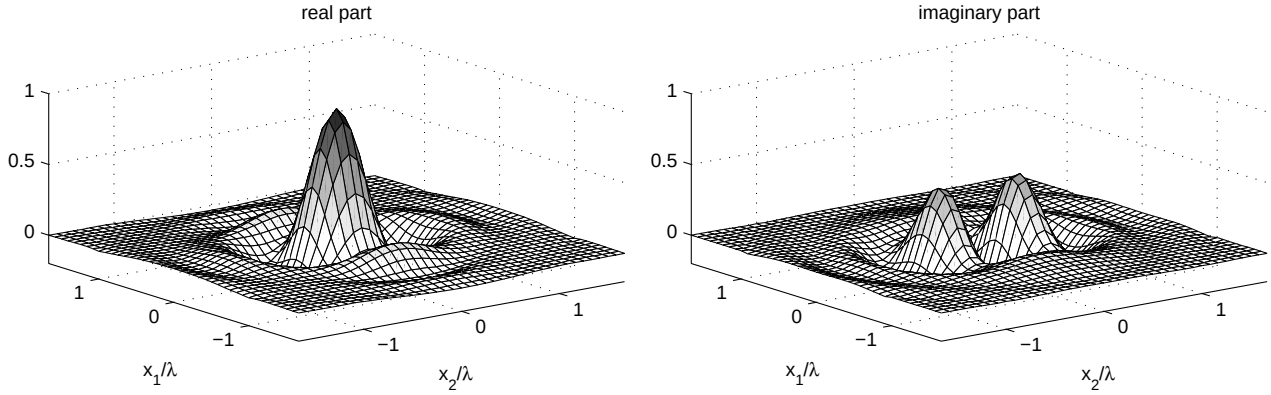

Figure 2: Real and imaginary part of the resolution function using the modified Gazdag imaging algorithm

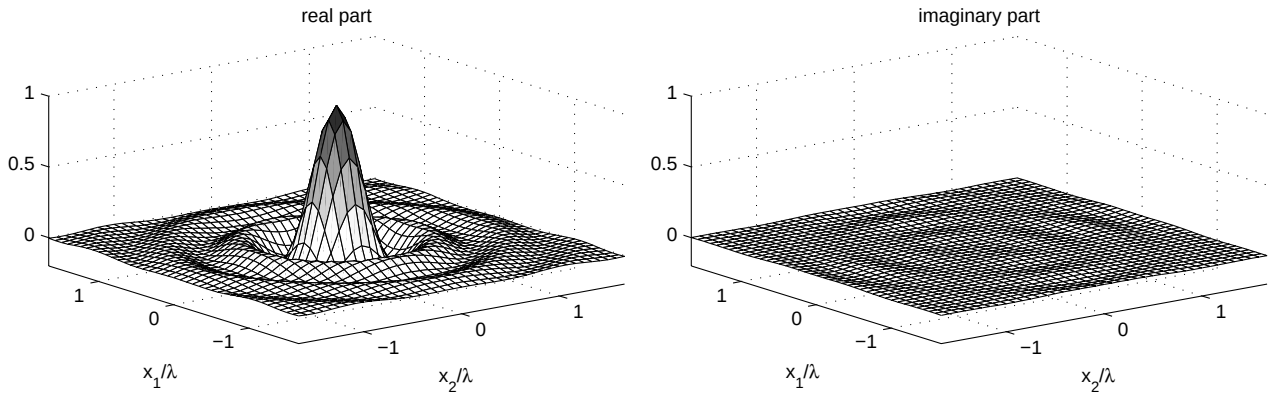

Figure 3: Real and imaginary part of the resolution function using the multi-component imaging algorithm

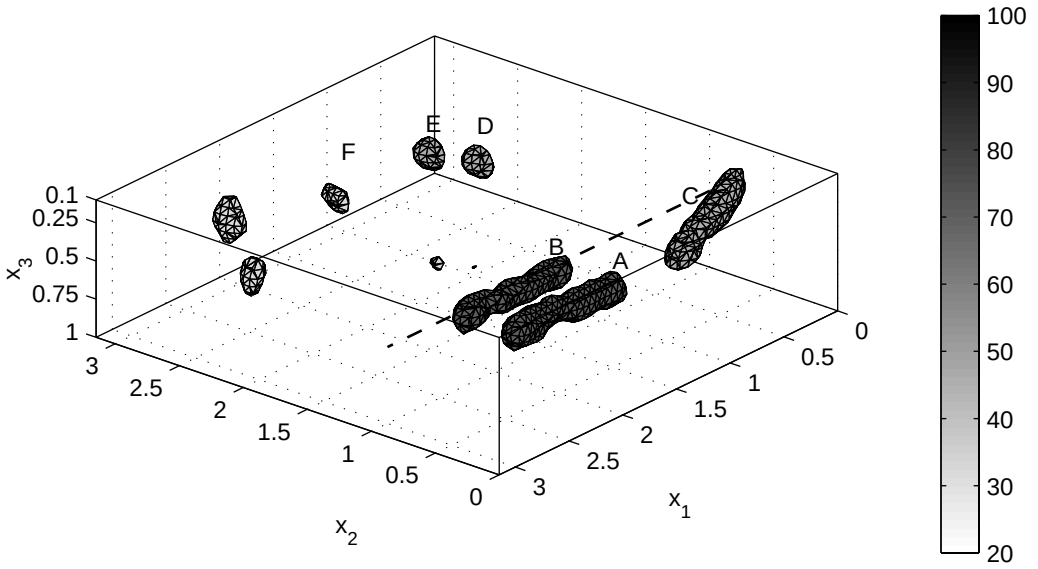

Figure 4: Multi-component imaging results using pE 900 MHz antennas

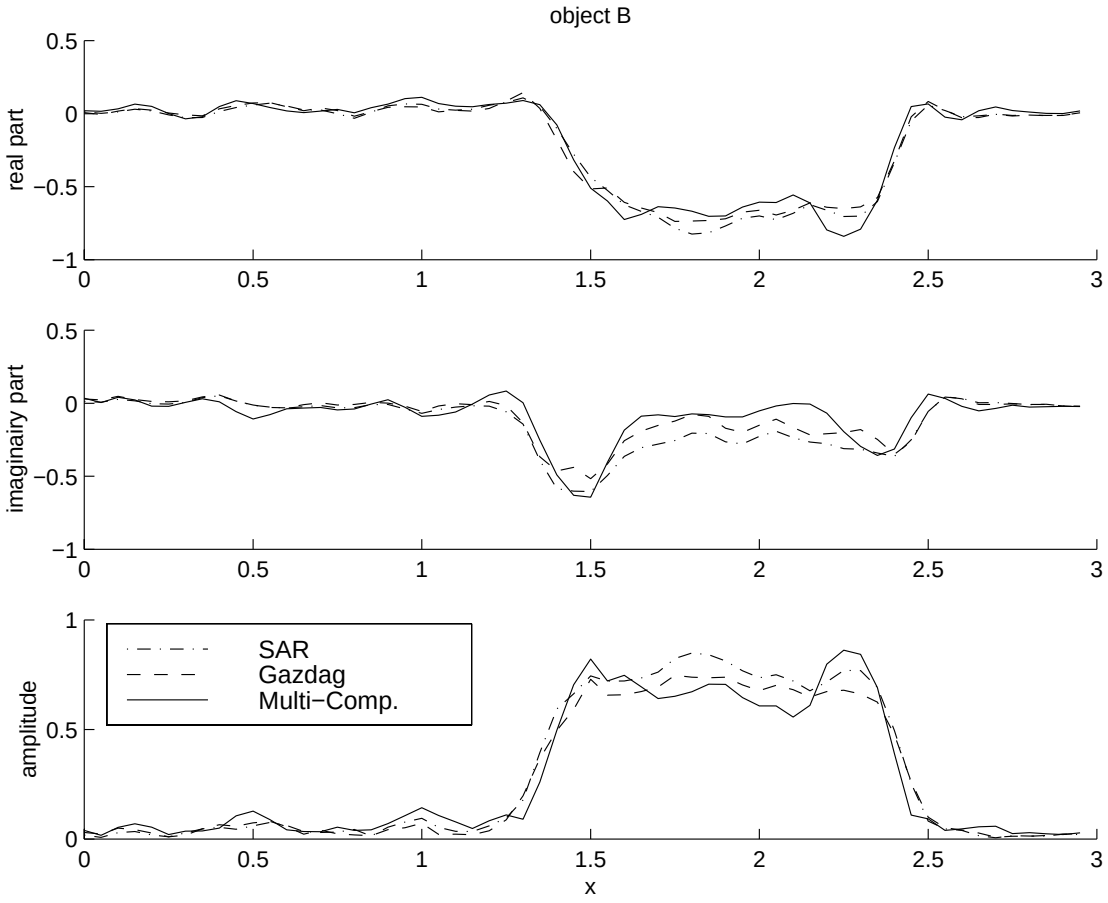

Figure 5: Comparison between SAR, Gazdag and multi-component imaging results along a line crossing object B parallel to the x_1 axis